Scaling Code-Multiplexed Electrode Networks for Distributed Coulter Detection in Microfluidics

Ruxiu Liu [a], Ningquan Wang [a], Norh Asmere [a], A. Fatih Sarioglu [a,b,c,*]

[a] School of Electrical and Computer Engineering, Georgia Institute of Technology, Atlanta, GA 30332, United States
[b] Petit Institute for Bioengineering and Biosciences, Georgia Institute of Technology, Atlanta, GA 30332, United States
[c] Institute of Electronics and Nanotechnology, Georgia Institute of Technology, Atlanta, GA 30332, United States

Abstract

Microfluidic devices can discriminate particles based on their properties and map them into different locations on the device. For distributed detection of these particles, we have recently introduced a multiplexed sensing technique called Microfluidic CODES, which combines code division multiple access with Coulter sensing. Our technique relies on micromachined sensor geometries to produce distinct waveforms that can uniquely be linked to specific locations on the microfluidic device. In this work, we investigated the scaling of the code-multiplexed Coulter sensor network through theoretical and experimental analysis. As a model system, we designed and fabricated a microfluidic device integrated with a network of 10 code-multiplexed sensors, each of which was characterized and verified to produce 31-bit orthogonal digital codes. To predict the performance of the sensor network, we developed a mathematical model based on communications and coding theory, and calculated the error rate for our sensor network as a function of the network size and sample properties. We theoretically and experimentally demonstrated the effect of electrical impedance on the signal-to-noise ratio and developed an optimized device. We also introduced a computational approach that can process the sensor network data with minimal input from the user and the demonstrated system-level operation by processing suspensions of cultured human cancer cells. Taken together, our results demonstrated the feasibility of deploying large-scale code-multiplexed electrode networks for distributed Coulter detection to realize integrated lab-on-a-chip devices.

Keywords: Coulter sensing; microfluidics; coding; multiplexing

1. Introduction

Lab-on-a-chip devices offer exciting opportunities for the analysis of biological samples as they combine precise manufacturing with microscale phenomena to deterministically screen a large number of cells based on traditional (Liu et al., 2013; Nwankire et al., 2015; Stott et al., 2010) and non-traditional biomarkers (Jing et al., 2015; Lin and Lee, 2008; Sarioglu et al., 2015). Specifically, these microfluidic platforms can be engineered to apply mechanical (Huang et al., 2004; Hyun et al., 2013), electrical (Doh and Cho, 2005; Gascoyne and Vykoukal, 2002), magnetic (Robert et al., 2011; Vojtisek et al., 2010) or chemical forces (Nagrath et al., 2007; Xu et al., 2009) to fractionate cell suspensions at a high-throughput by separating them based on contrast in their properties. From this perspective, such platforms can be considered as highly efficient microfluidic manipulators that can map cells to different locations on the chip based on the properties under investigation. Due to these precise and unique sample fractionation capabilities, lab-on-a-chip devices have been widely used for upstream sample preparation prior to analytical measurements using conventional laboratory instrumentation (Karabacak et al., 2014; Sarioglu et al., 2015).

Sample manipulation and cell discrimination capabilities of lab-on-a-chip devices can be used for quantitative measurements if these systems can be coupled with sensors that can quantify the spatial mapping performed by a microfluidic device. Microscopy has been the method of choice for acquiring particle position on the microscale (Du et al., 2006; Konry et al., 2011). Despite its convenience, microscopy introduces redundancy into system, producing large amounts of data at the expense of temporal resolution, and requires specialized high-speed cameras to capture fast hydrodynamic events in microfluidic devices. Such instrumentation needs typically tie the microfluidic chip to the lab infrastructure and limits its use in mobile settings. While cell phone based computational-imaging approaches (Feizi et al., 2016; Joh et al., 2017; Yang et al., 2018) allow microscopy to be performed in mobile settings, these systems do face challenges such as rigid field-of-view, requirement for optically transparent substrates, external components and throughput that can easily be addressed by developing an integrated system.

Different types of sensors have been integrated into microfluidic devices (Altintas et al., 2018; Byun et al., 2012; Gossett et al., 2012; Kartanas et al., 2017). Among these, electrical sensors have been the most common due to ease of fabrication, label-free operation, high signal-to-noise ratio, and ability to directly interface with external electronics (Altintas et al., 2018; Hu et al., 2017). Particularly, impedance-based detection (i.e., Coulter sensing) has been universally employed for the counting and sizing of particles in microfluidic systems (Coulter, 1956; DeBlois and Bean, 1970). Micromachined Coulter detectors have several advantages over conventional macroscale counterparts. First, microfluidic channel size (i.e., the aperture size) can be precisely tuned to achieve optimal sensitivity (Luo et al., 2014). Second, the sensor geometry of both the aperture (Balakrishnan et al., 2015; Javanmard and Davis, 2013) and the electrodes (Hong et al., 2012; Xie et al., 2017) can be patterned to produce signal patterns that can further be used to increase the signal-to-noise ratio (SNR), which is particularly useful in detecting small particles.

We have recently introduced the Microfluidic CODES technique (Liu et al., 2016; Liu et al., 2017; Wang et al., 2017) for distributed Coulter detection in microfluidic systems. Microfluidic CODES uses varying sensor geometries to produce impedance modulations in the form of signature waveforms at different locations on a microfluidic chip to electronically acquire the location of particles as they are processed on the chip in a multiplexed fashion. The key advantages of this approach over other detection schemes used in microfluidics are the ability (1) to acquire spatial information from different locations on the microfluidic chip, conventionally obtained through an external microscope, (2) to utilize simple electrodes instead of specialized sensors that utilize non-standard fabrication processes and/or exotic materials, and (3) to code-multiplex information onto a single time waveform creating a hardware platform that is not more complex than a Coulter counter, while ensuring successful recovery of multi-dimensional information through computation. As such, Microfluidic CODES provides a practical and scalable solution to acquire sample manipulations on a microfluidic chip all-electrically in an integrated and low-cost device.

The utility of our distributed sensing approach to create integrated lab-on-a-chip devices for complex assays increases with the number of on-chip nodes that can simultaneously be monitored. Therefore, in this paper, we investigate the scaling of code-multiplexed electrode networks to accommodate more Coulter sensors by theoretically and experimentally evaluating the challenges associated with such network expansion. Specifically, we model the electrical interface to the microfluidic chip as a telecommunications channel and utilize the coding theory not only to optimize the sensor waveforms but also to analyze the decoding performance by analytically calculating the error rate as a function of the network size and the sample properties. We also investigate the effects of the scaled network layout on the system sensitivity and optimize the electrode configuration accordingly. Finally, we develop an algorithm to process the scaled sensor network data and experimentally characterize the device performance using cell suspensions. Taken together, our work represents a foundation for the development of large-scale code-multiplexed electrical sensor networks to be used in distributed Coulter detection of particles manipulated in microfluidic devices in order to transform extensive sample manipulation capabilities of microfluidics into integrated lab-on-a-chip systems for quantitative sample analysis.

2. Materials and methods

As a model code-multiplexed Coulter sensor network, we developed a microfluidic chip with 10 code-multiplexed sensors (Fig. 1).

2.1 Digital Code-Set Generation

Two 31-bit *m*-sequences, 1010111011000111110011010010000 and 1011010100011101111100100110000, were generated using two linear-feedback shift-registers (both initialized at the state "10000") based on two 5th order primitive polynomials $x^5 + x^3 + 1$ and $x^5 + x^3 + x^2 + x + 1$, respectively. Resultant *m*-sequences and their cyclic-shifted versions were added using an XOR operation to generate 31-bit Gold Sequences. Among the 33 distinct

sequences generated, 10 31-bit Gold Sequences (1010111011000111110011010010000, 1011010100011101111100100110000, 0001101111011010001111110100000, 1100001100100011100110110110101, 0110110111100100010101100100101, 0000010011101110101110100011011, 0111001011010000110100110011110, 0100110010111001110110011101000, 0010010110110011001101011010110, 1001010001000000011111011111101) were chosen to construct the sensor network (Fig. 1a, 1b) presented in this work.

2.2 Microfabrication of the sensor

The device consists of a glass substrate with the microelectrode network and a polydimethylsiloxane (PDMS) with patterned microfluidic channels. The microelectrode network was fabricated using a lift-off process. A 1.5-µm thick negative photoresist (NR9-1500PY, Futurrex, Inc., Franklin, NJ) was patterned on a glass substrate through a chrome photomask using conventional lithography, followed by an electron-beam evaporation of 20 nm-thick Cr layer to promote adhesion and 80–480 nm-thick Au films as conductors. Sacrificial photoresist film was later etched in acetone under sonication to complete the electrode network fabrication. Microfluidic channels were fabricated using soft lithography. A 15-µm thick SU-8 negative photoresist (MicroChem, Westborough, MA) layer was spun on a 4-inch silicon wafer, and patterned with photolithography to create the mold. PDMS prepolymer and crosslinker (Sylgard 184, Dow Corning, Auburn, MI) were first mixed at a 10:1 ratio and was subsequently degassed in a vacuum desiccator. The mixture was poured onto the previously prepared mold and was cured in an oven at 65 °C for 4 hours. Cured PDMS was peeled off from the mold, cut into pieces using a scalpel, and fluid inlet and outlets holes were punched using a biopsy punch. The glass substrate with electrodes and the PDMS containing microfluidic channels were surface-activated in oxygen plasma, aligned under a microscope and bonded to complete the device fabrication process (Fig. 1).

2.3 Electronic Instrumentation

A 500 kHz sine wave was applied from the common electrode using a signal generator to excite the sensor network. To detect intermittent changes in the impedance between electrodes due to cells flowing in microfluidic channels, the electrical current between the common electrode and the other two electrodes were differentially measured. For this purpose, current signals from the two electrodes (i.e., representing different bit polarities in digital codes) were first converted into voltage signals using transimpedance amplifiers. Signals were subtracted from each other using a differential amplifier and root-mean-square (RMS) signal amplitude was measured using a lock-in amplifier (Zurich Instruments HF2LI). The lock-in amplifier demodulation bandwidth was specifically set at 2 kHZ to fully capture the dynamic impedance modulation due to cells flowing at speeds of 20-30 mm/s. Output signal from the lock-in amplifier was sampled into a computer using a data acquisition board (National Instruments BNC-2120) at 50 kHz. Recorded signals were post-processed and decoded using MATLAB through custom-developed algorithms, which will be explained later in the text (Fig. 1d).

2.4 Device Characterization

Human ovarian cancer cells (HeyA8) suspended in phosphate buffered saline (PBS) were used as biological samples to characterize the fabricated devices. Cells were cultured in RPMI 1640 (Mediatech; Cellgro, Herndon, VA) supplemented with 10% FBS (Fetal Bovine Serum; Seradigm, Radnor, PA) under 5% CO_2 atmosphere at 37 °C until they reached 80% confluence. The cells were then harvested and spiked into PBS to prepare the test solution.

Fabricated devices were characterized following the previously reported experimental setup (Liu et al., 2016). Briefly, the samples were driven through the devices using a syringe pump (Harvard PHD 2000) at a constant flow rate of 500 µL/h. Cell-sensor interaction was also optically recorded using an inverted microscope (Nikon Eclipse Ti-U) system equipped with a high-speed camera (Vision Research Phantom v7.3). Microscope images were post-processed to validate the electrical measurements when needed.

3. Results and discussion

3.1 Design and Operation

We implement code-division multiple access (CDMA) (Abu-Rgheff, 2007; Proakis, 1989; Rao and Dianat, 2005), a technique commonly employed in wireless communications, on a microfluidic chip to construct our multiplexed electrical sensor network for distributed detection of suspended particles across the microfluidic device via Coulter principle. For our purposes, the main advantages of the code-division multiplexing over other multiplexing strategies are (1) its ability to operate without an active control on the signal frequency or on the timing of different sensors, and (2) the capability to dynamically allocate resources to active sensors (i.e., the portion of the electrodes interacting with the flowing particles) based on the instantaneous network load. Because of these advantages, our code-based multiplexing strategy simplifies the design of the microfluidic chip and the interface electronics considerably by compressing the sensor network data into a single time waveform, and thereby eliminating the need to run dedicated traces to individual sensors in the network.

Our model device consists of parallel microfluidic channels aligned with the electrical sensor network formed by micromachined surface electrodes (Fig. 1a). The sensor network is made up of three micropatterned coplanar electrodes: two electrodes representing opposite bit polarities (i.e., 1 or 0) and a common electrode meandering in between to electrically drive the sensor network. The electrodes are arranged to form 10 distinct electrode patterns, each based on a uniquely assigned 31-bit Gold sequence chosen from the previously generated digital code-set (Fig. 1b). For each sensor, the sequence of coding electrodes determines the specific bit sequence to be encoded, while the common electrode is routed between coding electrodes spatially demarcating individual bits (Fig. 1c).

When particles suspended in electrolyte-filled microfluidic channels flow over the sensor network, electrical impedance between electrodes intermittently increases, which is detected by measuring the amplitude of the AC current in the sensor network using a lock-in amplifier (Fig. 1d). Because the extent of individual sensor code bits (i.e., coding electrode pitch) is specifically designed to be larger than the size of the particle to be detected, localized impedance changes between electrode pairs generate discrete pulses that are analogous to bits in a digital signal. Therefore, sequential interaction of the flowing particle with electrode pairs forming the sensor produces a signature time waveform of pulses dictated by the underlying spatial electrode pattern (Fig. 2). Moreover, the differential measurement of the current modulation between the common electrode and the two coding electrodes results in the polarity of the pulses switching between the two coding electrodes so that bipolar waveforms are produced.

3.2 Sensor Demultiplexing

The orthogonal signal waveforms generated by individual sensors in the network can be distinguished from each other with high SNR through a matched filter bank (Fig. 3a). For the decoding process, we first construct a set of code templates based on the averages of experimentally obtained sensor signals. Using these templates, we generate code waveforms broadened or compressed to account for different flow speeds of the particles. A matched filter bank is then constructed in MATLAB based on the whole template set and applied on the recorded signal.

When multiple cells simultaneously interact with the electrode network, individual sensor signals from those coincident cells interfere at the output signal. Interfering signals have random delays (due to asynchronous arrival of particles), and can have different amplitudes (due to different particle sizes) and durations (due to different particle flow speeds). In addition, the interference can be generated from particles interacting with different sensors (Fig. 3b) or with the same sensor (Fig. 3c). We can successfully demultiplex interfering sensor signals as we rely on the fact that pseudorandom noise (PRN) sequences (i.e., Gold sequences) ensure a sharp autocorrelation peak only when the template and the signal are completely aligned in time and sequence (Fig. 3a). Once an autocorrelation peak is identified, we subtract an estimate of the dominant sensor waveform from the signal to eliminate the crosstalk in detecting sensor signals with less power from smaller particles (Liu et al., 2016; Verdu, 1998).

Besides enabling the construction of a larger orthogonal code-set to expand the sensor network, longer codes yield higher sensitivity in identifying individual sensor signals in the presence of interference from others in the network. This is because, a matched decoder selectively amplifies the target signal (i.e., autocorrelation) while suppressing the other sensor signals as they appear as random noise to the decoder. This selective amplification, called CDMA processing gain, provides higher gain with longer code sequence. A comparison of decoder output from our device based on 31-bit Gold sequences with another system based on 7-bit Gold sequences, demonstrates the higher sensitivity (Fig. S1). Note that the signals obtained from relatively small cells are specifically chosen to demonstrate the effect of processing gain in suppressing the electronic noise.

3.3 Error Rate Estimation

Interference from one sensor appears as noise in the output of a decoder designed to receive signals from another sensor. Therefore, interference due to coincident particles leads to lower SNR and eventually leads to errors in decoding of the sensor network data. To theoretically calculate the error rate due to multiplexing, we model the sensor interference by first assuming individual sensor signals (s_k) as sequences of random bipolar pulses (c_k) mixed with the excitation signal at frequency f_c.

$$s_k(t) = \sqrt{2P_k}c_k(t)\cos(2\pi f_c t)\,, \tag{1}$$

$$c_k(t) = \sum_{i=0}^{N-1} c_{k,i}\Pi\left(\frac{t - iT_c}{T_c}\right), \quad c_{k,i} \in \{-1,1\}\,, \tag{2}$$

where P_k is the signal power from the k-th sensor, N is the number of bits in the digital code and $\prod(t)$ is the rectangular function that equals 1 for $0 < t < 1$ and 0 otherwise. For k coincident cells (Fig. 4a), the output I of the correlation decoder designed to receive the signal from the sensor with code c_0 is given by

$$I = \int_0^T c_0(t)\cos(2\pi f_c t)\left(\sum_{k=0}^{K-1}\sqrt{2P_k}c_k(t-\tau_k)\cos(2\pi f_c t)\right)\mathrm{d}t\,. \tag{3}$$

I may be divided into two parts and expressed as

$$I = I_0 + I_k = \sqrt{\frac{P_0}{2}}T + \frac{1}{2}\int_0^T\left(\sum_{k=1}^{K-1}\sqrt{2P_k}c_k(t-\tau_k)c_0(t)\right)\mathrm{d}t\,, \tag{4}$$

where I_0 is the desired contribution to the output from the "matched" sensor, I_k is the multiple access interference from all other sensors, and τ_k is the delay for the k-th sensor. Note that the delay τ_k is between the code waveforms while the AC signal from each sensor is in phase, unlike the carrier waves in wireless communication channel. The noise is not included in the calculations as the decoder performance is clearly interference limited.

Modeling of the interference between code-multiplexed information sources and its effect on the bit error rate have been studied extensively in the context of wireless communications (Holtzman, 1992a; Rappaport, 2002). We model the interference of k particles in our device with the Improved Gaussian Approximation (IGA) (Holtzman, 1992b; Liberti and Rappaport, 1995) which is used to analyze multi-access interference among k transmitters. In IGA, we model the variance of the interference as a Gaussian random variable (Ψ) with a mean μ_Ψ and a variance σ_Ψ^2, which are calculated as

$$\mu_\Psi = \frac{TN}{3}(K-1)\mu_p\,,$$

(5)

$$\sigma_\Psi^2 = (K-1)\frac{T^4}{4}\left[\left(\frac{7N^2+2N-2}{15}\right)\sigma_\mathrm{p}^2 + \left(\frac{1}{45}N^2 + \left(\frac{1}{9}K - \frac{4}{45}\right)N - \left(\frac{1}{9}K - \frac{4}{45}\right)\right)\mu_\mathrm{p}^2\right],$$

(6)

where μ_p and σ_p^2 are the mean and variance of the sensor signal power levels. We determine from our data on cell experiments (Fig. 4b) that $\sigma_p = 2.4\,\mu_p$. If we also assume that an error occurs when the interference random variable becomes larger than the desired signal, the error probability can be expressed as

$$\begin{aligned} P_{e0} &= E\left[Q\left(\sqrt{\frac{P_0T^2}{2\Psi}}\right)\right] \\ &\approx \frac{2}{3}Q\left(\sqrt{\frac{P_0T^2}{2\mu_\Psi}}\right) + \frac{1}{6}Q\left(\sqrt{\frac{P_0T^2}{2\left(\mu_\Psi+\sqrt{3}\sigma_\Psi\right)}}\right) + \frac{1}{6}Q\left(\sqrt{\frac{P_0T_b^2}{2\left(\mu_\Psi-\sqrt{3}\sigma_\Psi\right)}}\right). \end{aligned}$$

(7)

Because the error rate (P_e) is a function of the power of the target signal, average error probability is calculated by averaging Eq. 7 over all possible sensor signal power levels and is given by

$$P_e = \int_0^\infty P_{e0} f_{P_0}(P_0)\mathrm{d}P_0\,,$$

(8)

where f_{P_0} is the probability density function for sensor signal power levels. Using experimentally measured sensor power levels, we estimated the error rate as a function of expected coincident cells (Fig. 4c). In our system, the number of coincident cells can be modeled as a random variable (X) with Poisson distribution:

$$P(X=k) = \frac{e^{-\lambda}\lambda^k}{k!},$$

(9)

where λ is the expected number of coincident cells. The average error rate can be calculated as

$$E = \sum_{i=2}^{\infty} P_e(k)\frac{e^{-\lambda}\lambda^k}{k!}.$$

(10)

Because, the expected number of cells (λ) depends on the particle concentration (c) and the sensing volume (V) (i.e., $\lambda = c \times V$), average error rate can also be calculated as functions of sample and device properties (Fig. 4d). These results not only give us a theoretical estimate for

the device performance when processing different samples, but they also provide guidance in device design by demonstrating that sensor volume should be minimized to achieve lowest error rate for a given particle density. By the same token, the particle density can be tuned through dilution to achieve a target error rate for a given sensor network design.

3.4 Electrode Layout Optimization

Because code waveforms are generated through physical interaction between electrodes and flowing particles, the layout of electrodes needs to be optimized at both the individual sensor-level and the network-level to maximize performance.

At the sensor-level, the electrode pitch is an important parameter that determines the pulse duration, which corresponds to the "chip duration" (Glover and Grant, 1998; Rao and Dianat, 2005) in a conventional CDMA system. In our device, center-to-center distance between two common-electrode fingers defines the spatial extent of individual bits. When this distance is less than the particle size, inter-symbol interference occurs between adjacent bits and the code waveform is distorted. When the distance is larger than the particle size, there are two drawbacks: First, the baseline microfluidic channel impedance will be higher and therefore the SNR in the detection of impedance modulation due to particles will be lower. Second, spacious bits will result in larger sensors to implement the same code and therefore will lead to more cell coincidence and higher error rate. Therefore, the optimum solution to this trade-off is to design bits similar in size to the target particle. In our model device (Fig. 5a), we employed 5 μm-wide electrodes separated by 5 μm gaps to create a 20 μm bit size, specifically based on the 15 μm mean diameter of the target cell population.

At the network-level, the number of sensors and their locations determine the length of electrodes used in building the circuit, which needs to be optimized to minimize resistive losses. Inevitably, greater number of networked sensors encoding longer code sequences require more coding electrode pairs, resulting in longer electrode traces. Importantly, in our device layout, two sensing electrodes are placed freely and the common electrode is placed between two electrodes meanderingly to generate bipolar signals. As a result, the scaling of the sensor network leads to a dramatic increase in the length of the common electrode trace (Fig. 5a). In estimating the resulting electrode resistance, the minimum length of Gold sequences (i.e., # of bits, denoted by b)required to multiplex m sensors on the microfluidic chip can be calculated as

$$b = 2^n - 1\,, \tag{11}$$

where

$$n = \lceil \log_2(m-1) \rceil + \left\lfloor 1 - \frac{\lceil \log_2(m-1) \rceil - \left\lfloor \frac{\lceil \log_2(m-1) \rceil}{4} \right\rfloor \times 4}{4} \right\rfloor . \tag{12}$$

For an m-sensor network, with each sensor coded b bits using an array of $l \times w$ sized electrodes separated by a distance of g, the minimum length (L) of the common electrode can be parametrically expressed as

$$L = 2mb(w + g) + m\frac{b}{2}l\,. \tag{13}$$

This expression assumes an average of $\frac{b}{2}$ bit polarity changes ("01" or "10") in a b-bit long Gold sequence since it is a pseudorandom noise sequence. Each polarity change requires a common electrode crossover in the sensor geometry adding to the trace length (Fig. 5a). For a 10-sensor network constructed with 5-μm electrode fingers, the total length of the common electrode can be more than 20 mm, leading to the electrode resistance values on the order of tens of kiloohms (Fig. 5b).

We experimentally investigated the effects of the potential drop over the common electrode due to higher trace resistance using a device with sensors serially placed along a serpentine-patterned microfluidic channel. This analytical device configuration allowed us to directly compare signals from different sensors along the microfluidic path, since all sensors interacted with the same cell sequentially, eliminating the effects of size and electrical properties of the cell. When non-optimized, the signal power was observed to gradually decrease with increasing distance between the sensor and the driving voltage source (Fig. 5c, left). This is problematic for the device operation since (1) it reduces the SNR in measurements and risks weaker signals from farther sensors to be buried in noise, (2) it introduces artifacts in the output by creating a non-uniform sensitivity between sensors in the network, leading to bias in error rates.

To optimize the network design for signal uniformity among sensors, we systematically investigated the effects of the device geometry, film thickness and the electrode material in minimizing the common electrode resistance (Fig. S2). We optimized the device geometry in several ways. First, we increased the width of sections of the common electrode that fell outside of the microfluidic layout. Note that the width of the coding electrodes crossing the microfluidic channel remained unaltered to preserve the electrode pitch so that code waveform is generated without inter-symbol interference. Second, we shortened redundant parts of the electrodes that were specifically reserved to accommodate fabrication misalignment between the microfluidic layout and the coding electrodes. In addition to the structural modifications on the electrode network layout, we also applied the driving voltage from both ends of the common electrode trace, effectively halving the peak trace length. With these geometrical modifications alone, we were able to significantly reduce the signal variation among sensors (Fig. S2(a)). Next, we explored globally increasing the thickness of the electrode network. Because the resistivity of gold decreases nonlinearly with its thickness for a thin (~100 nm) layer of gold (Chopra et al., 1963), increasing the gold film thickness to 480 nm decreased the electrode trace resistance beyond what would be expected from geometrical scaling of the electrode cross section (Fig. S2(b)). Finally, we compared gold to platinum, another metal commonly used to build electrolyte-

interfacing sensors, as the electrode material and found that higher resistivity (~4.5×) of the platinum resulted in not only greater attenuation of signals with the trace length, but also a polarity-wise unbalanced response due to higher resistance mismatch between the two sensing electrodes (Fig. S2(c)). Combining these results, we developed an optimized device with significantly reduced trace resistance (Fig. 5b) that produced a uniform response among sensors in the network, demonstrating negligible voltage drop over the common electrode trace (Fig. 5c).

3.5 Processing of Microfluidic Sensor Network Data

From the perspective of the hardware setup and signal acquisition, our device operates very similar to a conventional Coulter counter, as the electrodes are driven by an AC source and the output waveform consists of fluctuations due to flowing particles intermittently changing the impedance between electrodes (Fig. S3). However, unlike a conventional Coulter counter, data from the network of coded Coulter counters (i.e., sensors) includes an additional layer of information and the output signal should be computationally analyzed to recover signals coming from different locations on the microfluidic chip.

To process sensor network data, we developed a LabVIEW program to implement custom decoding algorithms (Fig. 6a). In the program, the data signal, initially oversampled (50 kHz) to prevent aliasing, was first low-pass-filtered (with a cut-off frequency of 5 kHz) to eliminate the high frequency noise. The whole waveform was first analyzed to eliminate idle time frames with no sensor activity to increase the efficiency of the decoding process. To identify idle time frames, the zero-crossing rate (ZCR) was used as the discrimination parameter, as ZCR for noise is expected to be greater than that of sensor signals. Specifically, ZCR was calculated for every 200 samples (20% of the estimated particle transit time), and only time frames with ZCR < 0.2 were considered as sensor-active time frames (containing sensor signals).

Next, sensor-active time frames were analyzed to create a template library based on the recorded sensor signals. In this process, we provided the set of digital codes implemented in the device, dimensions of the microfluidic device and the volumetric flow rate of the sample to the program, which used these parameters to automatically search the acquired data for the sensor signal waveforms. A waveform was only scored as a template waveform if (1) it produced a dominant correlation peak with only one of the codes in the provided codeset (i.e., the amplitude of the largest correlation peak was more than twice of that of the secondary correlation peak) and (2) the waveform duration was in agreement with the one calculated based on the expected particle flow speed (i.e., the signal duration was within 150% of the estimated signal duration). These conditions guaranteed that only non-interfering waveforms due to target particles were considered in template generation. Scored waveforms were then clustered for individual sensors, and when the program accumulated enough (n>20) waveforms for each sensor, time- and power-normalized waveforms were averaged to obtain the templates. Construction of the template library based on the experimental data is important as it allowed us to accommodate variations in the signal due to artifacts in device fabrication.

Once the template library was established, we processed the recorded sensor network data using a decoding algorithm based on the successive cancellation of interfering signals (Liu et al., 2016; Liu et al., 2017; Wang et al., 2017). Sensor-active time frames were transferred from the previous step, and the prolonged ones (with a duration greater than 5× of the expected particle transit time) were divided into shorter time frames. Then all time frames were down-sampled by 5× to increase the decoding efficiency and then analyzed individually using successive interference cancellation. Each time frame was first compared with the template library through correlation, and the largest correlation peak and the matching template were used to reconstruct the signal with the most power. Following the subtraction of the estimated signal from the signal frame, the algorithm recursively searched for the coincident sensor signals by eliminating the strongest signal until the correlation of the residual signal with the template library could not exceed a predetermined threshold value. At the end of the process, the original output waveform can be decomposed into data streams from individual sensors (Fig. 6b). These data not only include the locations of the particles on the microfluidic chip based on the unique sensor waveform but also provides information on the size and the speed of each particle based on the signal amplitude and duration, respectively.

4. Conclusion

Microfluidic CODES is a platform technology that enables distributed Coulter detection of particles across a microfluidic chip. It employs sensors micromachined to generate distinct waveforms that can uniquely be linked to different locations on a microfluidic chip for a code-multiplexed readout. The number of code-multiplexed sensors can be increased to enhance the utility of this sensing approach by designing individual sensors to generate signals that are computationally distinguishable from each other. Interference among code-multiplexed Coulter sensors increases with the network size decreasing the SNR and therefore, the sample concentration should be adjusted to achieve a target error rate for a given size of the network. Design and physical implementation of the scaled sensor network should also prioritize minimization of the electrode trace resistance to ensure uniform response from the sensors in the network. The theoretical, experimental and the algorithmic framework established in this paper will enable the development of distributed Coulter sensor networks with higher complexity. The future work will involve the combination of the Microfluidic CODES technology with microfluidic sample manipulation to implement all-electronic and fully integrated lab-on-a-chip assays for a variety of applications.

ACKNOWLEDGEMENT

This work was supported by National Science Foundation Award No. ECCS 1610995, National Science Foundation CAREER Award No. ECCS 1752170, and the Beckman Young Investigator Award (to A.F.S.).

REFERENCES

Abu-Rgheff, M.A., 2007. Introduction to CDMA wireless communications, Academic Press, Oxford.
Altintas, Z., Akgun, M., Kokturk, G., Uludag, Y., 2018. Biosens. Bioelectron., 100, 541-548.
Byun, S., Son, S., Amodei, D., Cermak, N., Shaw, J., Kang, J.H., Hecht, V.C., Winslow, M.M., Jacks, T., Mallick, P., Manalis, S.R., 2013. Proc. Natl. Acad. Sci. U. S. A., 110 (19), 7580-7585.
Balakrishnan, K.R., Whang, J.C., Hwang, R., Hack, J.H., Godley, L.A., Sohn, L.L., 2015. Anal. Chem., 87 (5), 2988-2995.
Chopra, K.L., Bobb, L.C., Francombe, M.H., 1963. J. Appl. Phys. 34 (6), 1699-1702.
Coulter, W.H., 1956. Proc. Natl. Electron. Conf., 12, 1034-1040.
DeBlois, R.W., Bean, C.P., 1970. Rev. Sci. Instrum., 41, 909-916.
Doh, I., Cho, Y.H., 2005. Sens. Actuators A, 121 (1), 59-65.
Du, Z., Colls, N., Cheng, K.H., Vaughn, M.W., Gollahon, L., 2006. Biosens. Bioelectron., 21 (10), 1991-1995.
Feizi, A., Zhang, Y., Greenbaum, A., Guziak, A., Luong, M., Chan, R.Y.L., Berg, B., Ozkan, H., Luo, W., Wu, M., Wu, Y., Ozcan, A., 2016. Lab Chip 16 (22), 4350-4358.
Gascoyne, P.R.C., Vykoukal, J., 2002. Electrophoresis, 23 (13), 1973-1983.
Gossett, D.R., Tse, H.T.K., Lee, S.A., Ying, Y., Lindgren, A.G., Yang, O.O., Rao, J., Clark, A.T., Di Carlo, D., 2012. Proc. Natl. Acad. Sci. U. S. A., 109 (20), 7630-7635.
Glover, J.G., Grant, P.M., 1998. Digital Communications, Prentice Hall Europe, London.
Holtzman, J.M., 1992a. IEEE Trans. Commun., 40 (3), 461-464.
Holtzman, J.M., 1992b. IEEE Trans. Autom. Control, 37 (2), 243-247.
Hong, J.L., Lan, K.C., Jang, L.S., 2012. Sens. Actuators B, 173, 927-934.
Hu, C., Kalsi, S., Zeimpekis, I., Sun, K., Ashburn, P., Turner, C., Sutton, J.M., Morgan, H., 2017. Biosens. Bioelectron., 96, 281-287.
Huang. L.R., Cox, E.C., Austin, R.H., Sturm, J.C., 2004. Science, 304 (5673), 987-990.
Hyun, K.A., Kwon, K., Han, H., Kim, S.I., Jung, H.I., 2013. Biosens. Bioelectron., 40 (1), 206-212.
Javanmard, M., Davis, R.W., 2013. IEEE Sens. J., 13 (5), 1399-1400.
Jing, T., Ramji, R., Warkiani, M.E., Han., J., Lim, C.T., Chen., C.H., 2015. Biosens. Bioelectron., 66, 19-23.
Joh, D.Y., Hucknall, A.M., Wei, Q., Mason, K.A., Lund, M.L., Fontes, C.M., Hill, R.T., Blair, R., Zimmers, Z., Achar, R.K., Tseng, D., Gordan, R., Freemark, M., Ozcan, A., Chilkoti, A., 2017. Proc. Natl. Acad. Sci. U. S. A. 114 (34), E7054-E7062.
Karabacak, N.M., Spuhler, P.S., Fachin, F., Lim, E.J., Pai, V., Ozkumur, E., Martel, J.M., Kojic, N., Smith, K., Chen, P.I., Yang, J., Hwang, H., Morgan, B., Trautwein, J., Barber, T.A., Stott, S.L., Maheswaran, S., Kapur, R., Haber, D.A., Toner, M., 2014. Nat. Protoc., 9 (3), 694-710.
Kartanas, T., Ostanin, V., Challa, P.K., Daly, R., Charmet, J., Knowles, T.P.J., 2017. Anal. Chem., 89 (22), 11929-11936.
Korny, T., Dominguez-Villar, M., Baecher-Allan, C., Hafler, D.A., Yarmush, M.L., 2011. Biosens. Bioelectron., 26 (5), 2707-2710.
Liberti, J.C., Rappaport, T.S., 1995. IEEE Global Telecommunications Conference, GLOBECOM ’95, 33-37.

Lin Y.H., Lee, G.B., 2008. Biosens. Bioelectron., 24 (4), 572-578.
Liu, R., Wang, N., Kamili, F., Sarioglu, A.F., 2016. Lab Chip 16 (8), 1350-1357.
Liu, R. Waheed, W., Wang, N., Civelekoglu, O., Boya, M., Chu, C.H., Sarioglu, A.F., 2017. Lab Chip, 17 (15), 2650-2666.
Liu, Z., Zhang, W., Huang, F., Feng, H., Shu, W., Xu, X., Chen, Y., 2013. Biosens. Bioelectron., 47, 113-119.
Luo, L., German, S.R., Lan, W.J., Holden, D.A., Mega, T.L., White, H.S., 2014. Annu. Rev. Anal. Chem., 7, 513-535.
Nagrath, S., Sequist, L.V., Maheswaran, S., Bell, D.W., Irimia, D., Ulkus, L., Smith M.R., Kwak, E.L., Digumarthy, S., Muzikansky, A., Ryan, P., Balis, U.J., Tompkins, R.G., Haber, D.A., Toner, M., 2007. Nature, 450 (7173), 1235-1239.
Nwankire, C.E., Venkatanarayanan, A., Glennon, T., Keyes, T.E., Forster, R.J., Ducree, J., 2015. Biosens. Bioelectron., 68, 382-389.
Proakis, J.G., 1989. Digital Communications, McGraw-Hill, New York.
Rao, R., Dianat, S., 2005. Basics of Code Division Multiple Access (CDMA), SPIE.
Rappaport, T.S., 2002. Wireless Communications: Principles and Practice, second ed., Prentice Hall, New Jersey.
Robert, D., Pamme, N., Conjeaud, H., Gazeau, F., Iles, A., Wilhelm, C., 2011. Lab Chip, 11 (11), 1902-1910.
Sarioglu, A.F., Aceto, N., Kojic, N., Donaldson, M.C., Zeinali, M., Hamza, B., Engstrom, A., Zhu, H., Sundaresan, T.K., Miyamoto, D.T., Luo, X., Bardia, A., Wittner, B.S., Ramaswamy, S., Shioda, T., Ting, D.T., Stott, S.L., Kapur, R., Maheswaran, S., Haber, D.A., Toner, M., 2015. Nat. Methods 12 (7), 685-691.
Stott, S.L., Hsu, C.H., Tsukrov, D.I., Yu, M., Miyamoto, D.T., Waltman, B.A., Rothenberg, S.M., Shah, A.M., Smas, M.E., Korir, G.K., Floyd Jr., F.P., Gilman, A.J., Lord, J.B., Winokur, D., Springer, S., Irimia, D., Nagrath, S., Sequist, L.V., Lee, R.J., Isselbacher, K.J., Maheswaran, S., Haber, D.A., Toner, M., 2010. Proc. Natl. Acad. Sci. U. S. A. 107 (43), 18392-18397.
Verdu, S., 1998. Multiuser detection, Cambridge University Press, Cambridge.
Vojtíšek, M., Iles, A., Pamme, N., 2010. Biosens. Bioelectron., 25 (9), 2172-2176.
Wang, N., Liu, R., Sarioglu, A.F., 2017. J. Vis. Exp., 121, e55311.
Xie, P., Cao, X., Lin, Z., Talukder, N., Emaminejad, S., Javanmard, M., 2017. Sens. Actuators A, 241, 672-680.
Xu, Y., Phillips, J.A., Yan, J., Li, Q., Fan, Z.H., Tan, W., 2009. Anal. Chem., 81 (17), 7436-7442.
Yang, K., Wu, J., Peretz-Soroka, H., Zhu, L., Li, Z., Sang, Y., Hipolito, J., Zhang, M., Santos, S., Hillier, C., de Faria, R.L., Liu, Y., Lin, F., 2018. Biosens. Bioelectron., 99, 259-267.

Figures

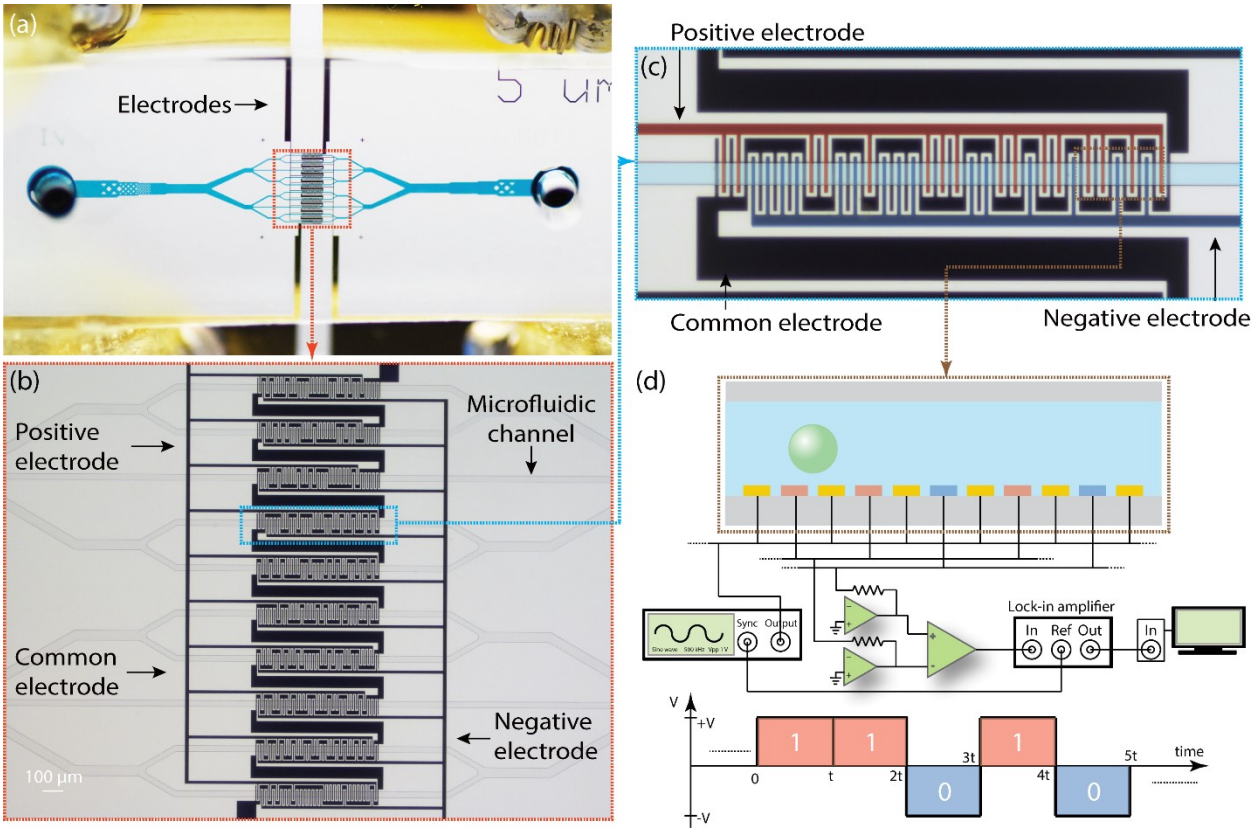

Fig 1 Code-multiplexed Coulter sensor network (Microfluidic CODES) layout and working principle. (a) A photo of the microfluidic device integrated with a network of 10 code-multiplexed sensors. The microfluidic chip is fabricated using soft lithography on a glass slide with micropatterned Au electrodes. The microfluidic channel layer is filled with a blue dye for imaging purposes. (b) Microscope image of the surface electrode network forming 10 Coulter sensors, each encoding a different 31-bit Gold sequence. The image also demonstrates the alignment of the glass substrate patterned with coded electrodes with the PDMS microfluidic channel layer. (c) A false-colored close-up image of one of the sensors in the network. Red and blue colored electrodes represent opposite bit polarities (1 and 0, respectively). The specific sensor in the image is designed to encode “1100001100100011100110110110101”. (d) A schematic illustrating the working principle and the measurement setup. When a particle flows over the coded electrode sequence, transient changes in the microfluidic channel impedance produce a sequence of pulses in the current signal. A bipolar signal is produced with a differential amplifier at the output of a lock-in amplifier.

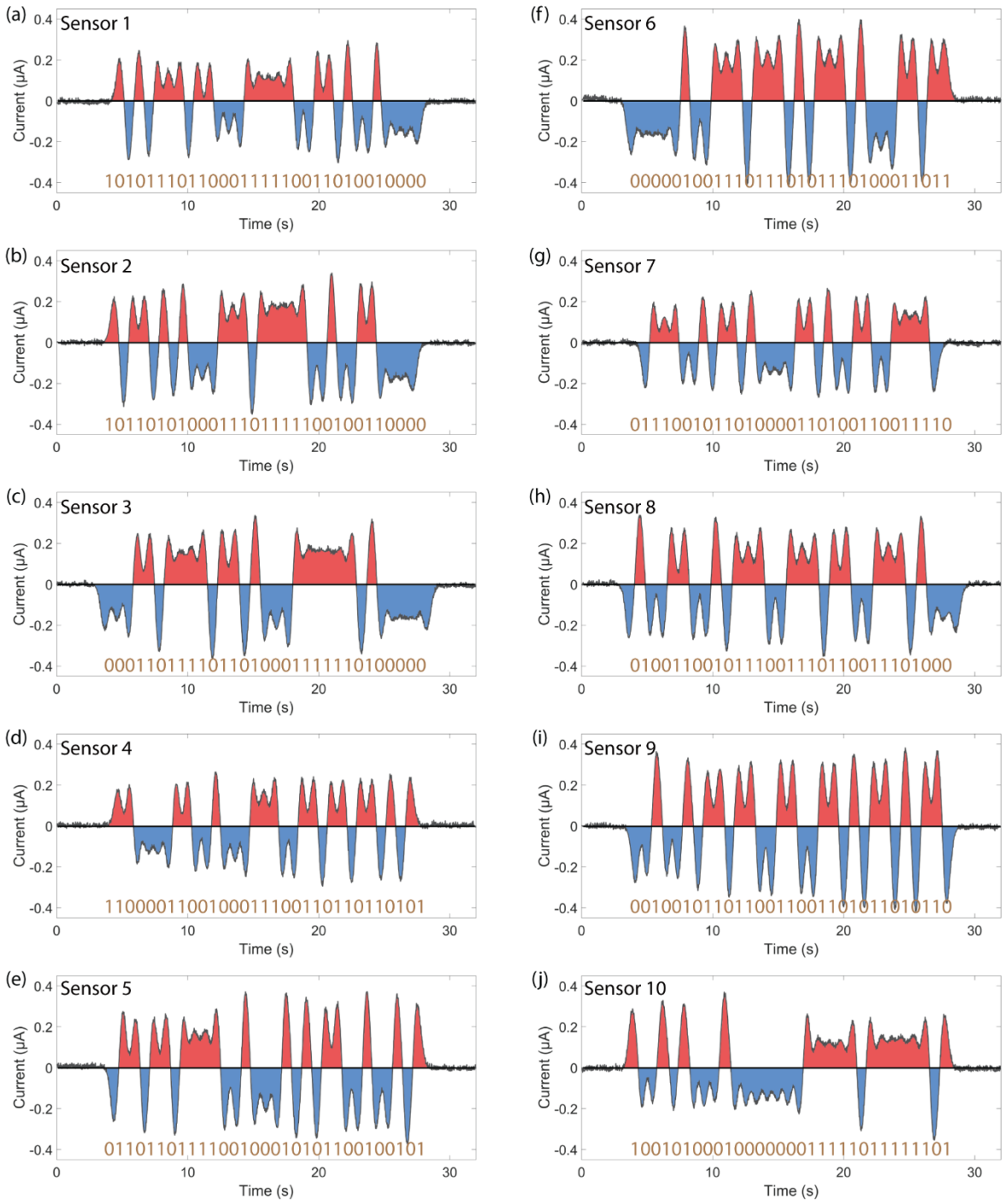

Fig 2 Representative individual sensor signals recorded from each of the 10 sensors in the network. In each signal, positive values are interpreted as “1” while negative values represent “0”. For each sensor, the output signal closely follows the specific bit sequence of the 31-bit Gold sequence encoded by the sensor. Corresponding digital code sequences for the signals shown in the figure are: (a) 1010111011000111110011010010000, (b) 1011010100011101111100100110000, (c) 0001101111011010001111110100000, (d) 1100001100100011100110110110101, (e) 0110110111100100010101100100101, (f)

00000100111011101011100100011011, (g) 01110010110100001101001100111110, (h) 01001100101110011101100111010000, (i) 00100101101100110011010110101110, (j) 10010100010000000111110111111101.

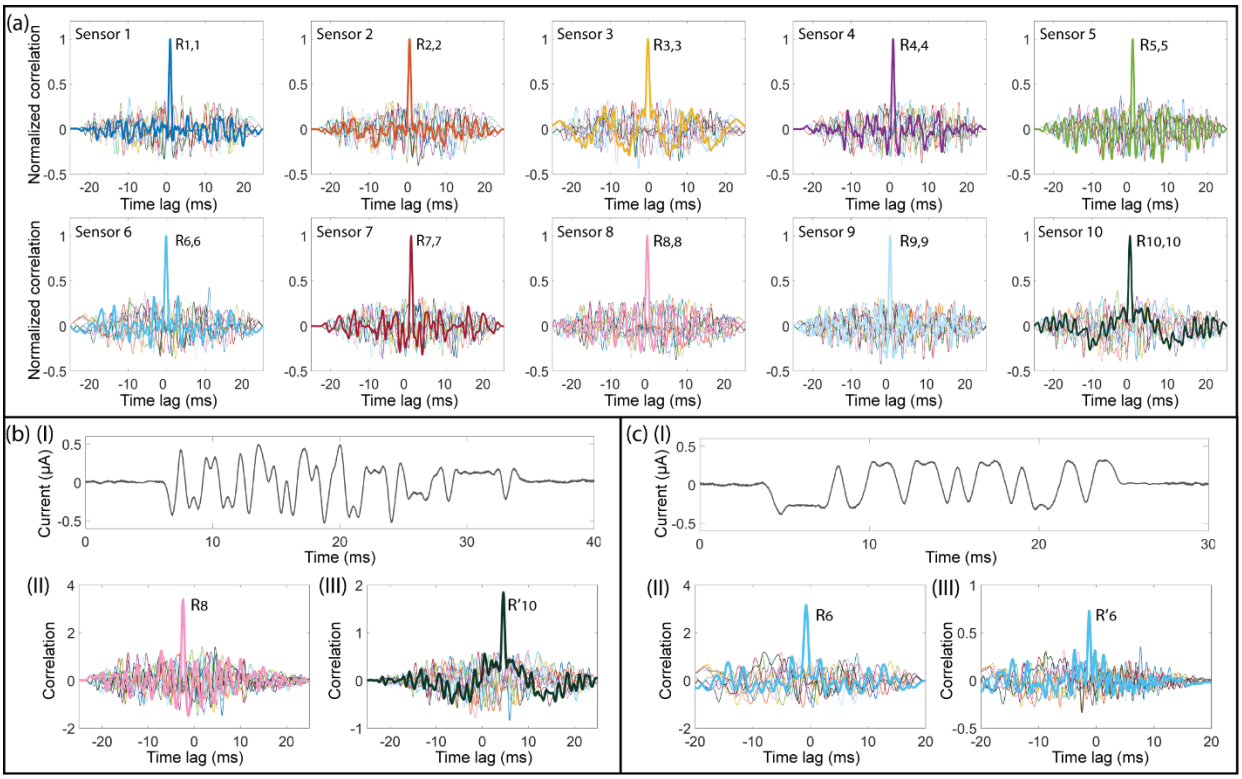

Fig 3 Demultiplexing of coded sensor signals through correlation analysis. (a) Sensor signals are correlated with a template library consisting of representative signals from all sensors in the network. Figures show results for 10 different sensor signals from their correlation with the template library for different time delays. A dominant autocorrelation peak at zero-time delay can be easily identified in each case, because the code sequences are specifically designed to be orthogonal to each other. Coincident particles lead to interference of signals from (b) different sensors or (c) the same sensor. Correlating the interference signal (I) with the template library produces a dominant peak that corresponds to the largest particle (II). Estimated signal for the largest cell is subtracted from the original signal and the residual signal is correlated with the template library again to recover the sensor signal due to next largest particle (III).

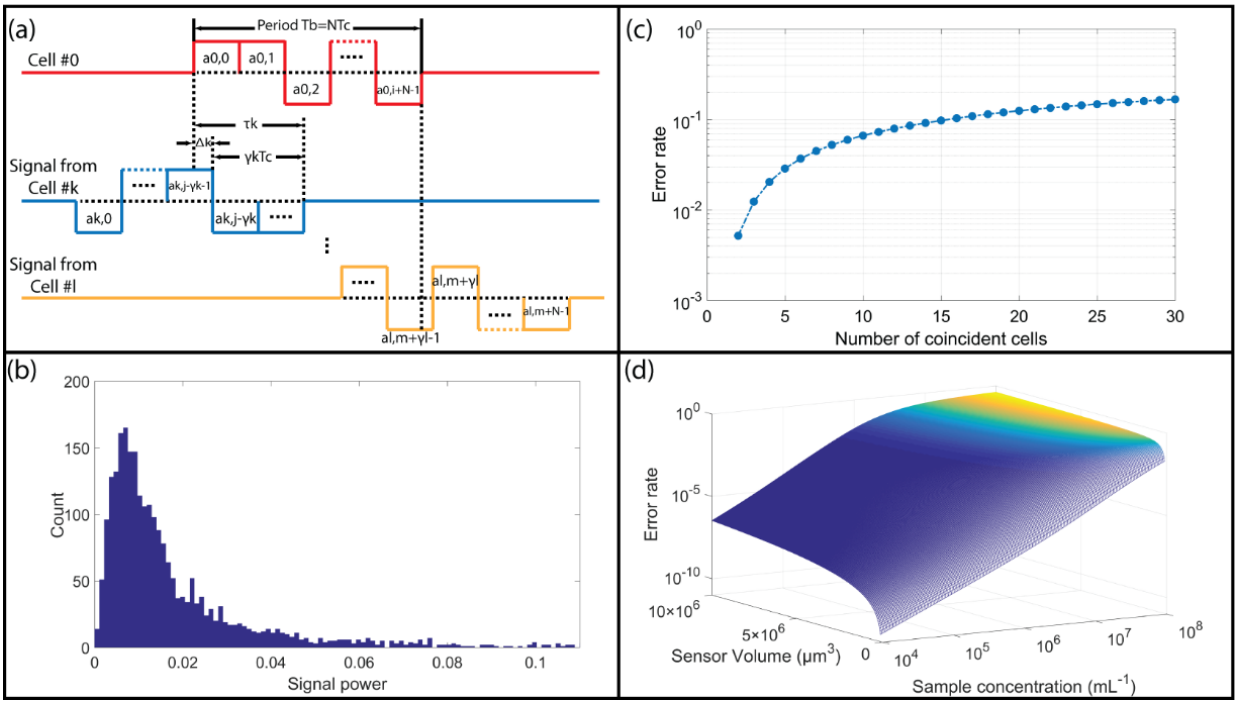

Fig 4 Theoretical analysis of the effect of sensor signal interference due to coincident cells on the decoder performance. (a) Mathematical framework to model sensor signal interference. Sensor signals are assumed to be digital waveforms with random delays between interfering signals. (b) The histogram showing the distribution of the sensor signal power from the sensor network interacting with a cell population. (c) The estimated bit error rate in the decoder as a function of the number of coincident cells. (d) The estimated bit error rate in the decoder as a function of the sample concentration (i.e., number of particles per unit volume) and the sensor network size (i.e., the total volume of liquid monitored by the sensor network).

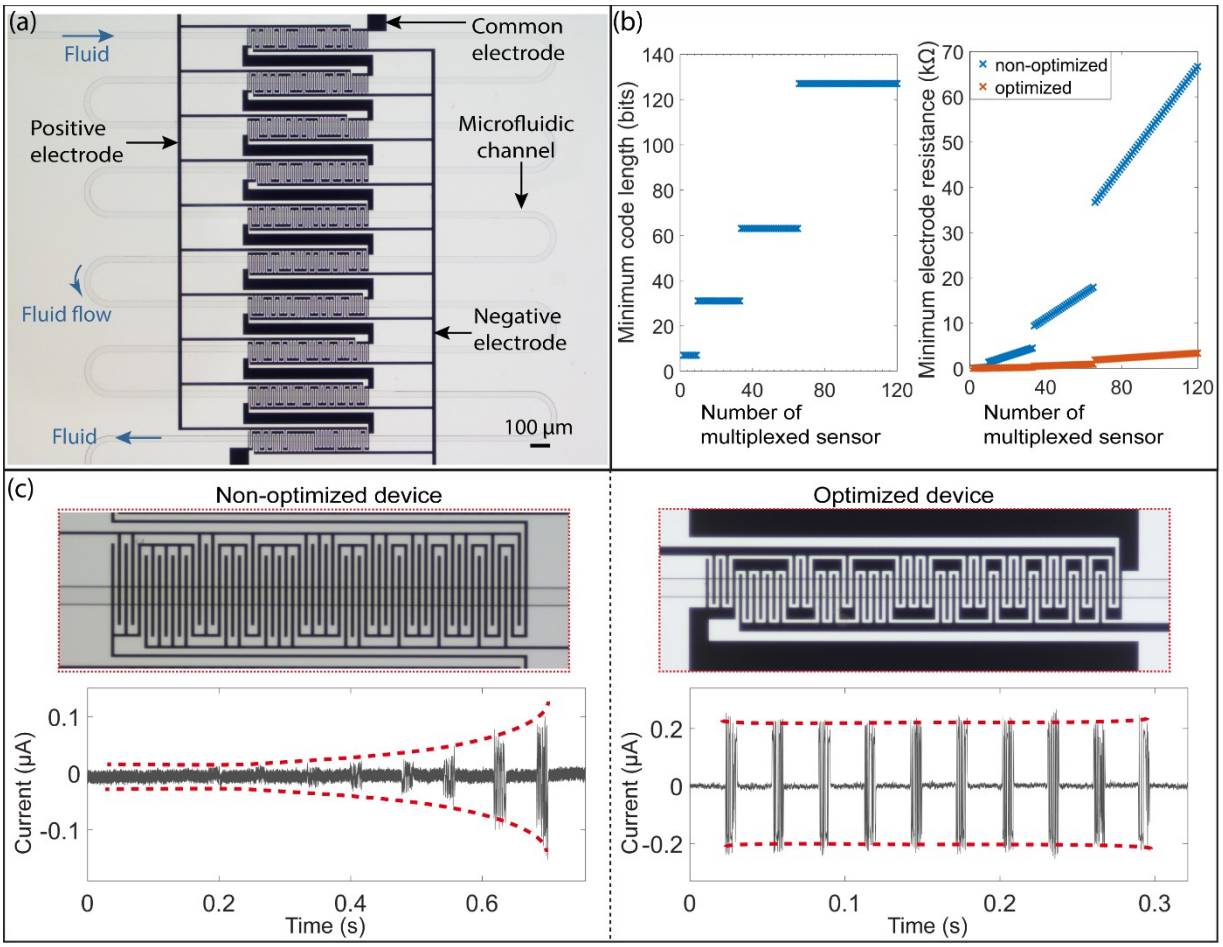

Fig 5 Optimization of the sensor network layout to maximize signal-to-noise ratio. (a) An image of the microfluidic device used to characterize the performance of different sensor network layouts. A serpentine microfluidic channel in the device ensures all sensors in the network to interact with the same particle. (b) Calculated minimum Gold code length (# of bits) (left) and the minimum common electrode resistance required to implement such a code (right) for both non-optimized (blue) and optimized (red) devices as a function of the number of multiplexed sensors in the sensor network. (c) Close-up images and the recorded sensor signals of a representative sensor layout in non-optimized (left) and optimized (right) devices. Comparison of waveforms shows the improvement in sensor signal uniformity achieved by optimized design.

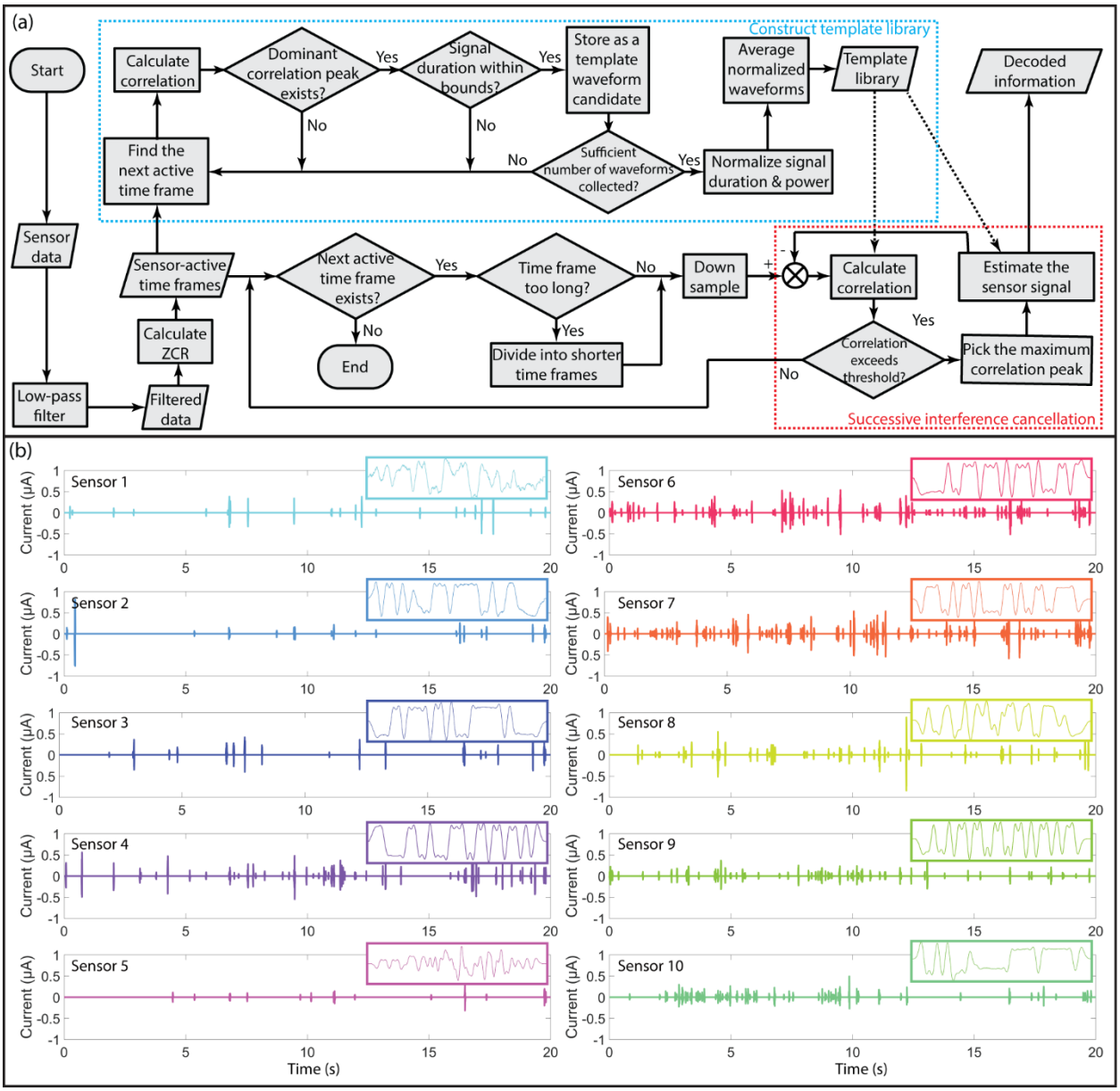

Fig 6 Computational processing of sensor signals to recover individual sensor signals. (a) The schematic showing the process flow of the developed decoding software. Following filtering of the input signal, templates are automatically obtained from the input signal. Waveform is divided into time blocks, which are individually correlated with templates. A successive interference cancellation algorithm iteratively decodes the interfering signals starting from the sensor signal with highest power. (b) The signals generated by each sensor in the network are recovered from an arbitrarily chosen 20-second-long waveform (See Fig. S3). Individual sensor waveforms reconstructed based on the correlation amplitude and the matching template are illustrated. Templates used to recover sensor signals are also provided for each sensor waveform.